POCSENSE: POCS-Based Reconstruction for Sensitivity Encoded Magnetic Resonance Imaging

Alexei A. Samsonov,[1*] Eugene G. Kholmovski,[2] Dennis L. Parker,[2] and Chris R. Johnson[1]

A novel method for iterative reconstruction of images from undersampled MRI data acquired by multiple receiver coil systems is presented. Based on Projection onto Convex Sets (POCS) formalism, the method for SENSitivity Encoded data reconstruction (POCSENSE) can be readily modified to include various linear and nonlinear reconstruction constraints. Such constraints may be beneficial for reconstructing highly and overcritically undersampled data sets to improve image quality. POCSENSE is conceptually simple and numerically efficient and can reconstruct images from data sampled on arbitrary *k*-space trajectories. The applicability of POCSENSE for image reconstruction with nonlinear constraining was demonstrated using a wide range of simulated and real MRI data. Magn Reson Med 52:1397–1406, 2004. © 2004 Wiley-Liss, Inc.

Key words: MRI; parallel imaging; image reconstruction; POCS; POCSENSE

Recently developed parallel MRI (P-MRI) techniques (1–10) may provide significant MRI acquisition speedup for imaging with multiple receiver coils. The speedup is attained by acquiring undersampled representations of *k*-space. The dissimilarities in coil sensitivities provide supplementary spatial encoding called sensitivity encoding. The image reconstruction from the reduced data sets requires additional calibration information, such as coil sensitivity profiles, or extra reference *k*-space lines (7,8). P-MRI could be applied with standard pulse sequences, and the attained speedup could be used for improving temporal and/or spatial resolution of MRI. Recent advances in sensitivity encoding allowed P-MRI with arbitrary *k*-space sampling trajectories (11).

P-MRI techniques provide a number of benefits in many practical applications. However, there are inherent difficulties when the P-MRI techniques are applied for image recovery from highly undersampled data sets. In such situations, the image reconstruction often becomes ill-conditioned, which may result in considerable degradation of the image quality by amplified noise. The effects can be partially resolved by conditioning the data inversion (6). Some P-MRI techniques (1,7,8) possess inherent numerical conditioning. The price of such conditioning is decreased reconstruction accuracy that may result in incomplete removal of aliasing arising from data undersampling. Advanced approaches (12–16) utilize adaptive regularization to minimize both power of aliasing artifacts and noise power. The method proposed in Ref. (12) uses low-resolution reference data to find optimal trade-off between the noise amplification and residual aliasing. Low-resolution reference scans were also used to achieve acceptable results for underdetermined SENSitivity Encoding (SENSE) reconstruction (16). The techniques presented in Refs. (14,15) rely on postreconstruction noise filtering to obtain a reference image for adaptive regularization in the second pass reconstruction.

All described methods exploit linear algebra framework to utilize additional information for image quality improvement. Another way to include a priori information into reconstruction is to use Projections onto Convex Sets (POCS) formalism. POCS is a powerful mathematical tool for reconstruction of incomplete and/or inconsistent data. POCS could be used in such situations due to its remarkable flexibility in constraint manipulation (17,18). Example applications of the POCS method in MRI include image reconstruction from partial *k*-space data (19–21), a reduction of image degradation caused by motion artifacts (22–24), and a correction of ghosting artifacts in EPI images (25). Applicability of POCS formalism to P-MRI data reconstruction problem has not been considered by the medical imaging community yet. However, such an approach to the problem solution would provide a valuable tool for utilization of various nontrivial constraints to achieve improved image quality.

In this paper, we propose a novel method for image reconstruction from sensitivity encoded MRI data. The new technique, POCSENSE, is based on the POCS formalism and provides an algorithmically simple and computationally efficient way to utilize various linear and nonlinear constraints in image reconstruction. The paper is organized as follows. In the first section, we give a brief overview of the POCS formalism and present sequential and parallel POCS approaches. Next, we describe our method and its implementation for Cartesian and non-Cartesian *k*-space trajectories. Finally, we present and discuss results of the application of POCSENSE to reconstruction of synthetic and real MRI data.

THEORY

POCS Reconstruction of MRI Data

The conceptual basis of POCS is that available constraints onto the solution of the image reconstruction problem can

[1]Scientific Computing and Imaging Institute, University of Utah, Salt Lake City, Utah.

[2]Utah Center for Advanced Imaging Research, Department of Radiology, University of Utah, Salt Lake City, Utah.

Grant sponsor: NIH BISTI; Grant number:1P20HL68566–01; Grant sponsor: NIH NCRR; Grant number: P41RR12553–05; Grant sponsor: NIH; Grant number: RO1 HL48223, RO1 HL53596.

*Correspondence to: Alexei A. Samsonov, Scientific Computing and Imaging Institute, University of Utah, 50 S. Central Campus Drive, Room 3490, Salt Lake City, UT 84112. Email: samsonov@sci.utah.edu

Received 31 March 2004; revised 29 July 2004; accepted 29 July 2004.

DOI 10.1002/mrm.20285

Published online in Wiley InterScience (www.interscience.wiley.com).

© 2004 Wiley-Liss, Inc.

be considered convex sets[3] in a Hilbert space, H, where H consists of all possible complex images. Every known constraint onto an image restricts it to lie in the associated closed convex subset of H. If m such constraints are available, then m closed convex sets Ω_i ($i = 1,2, \ldots, m$) may be defined. Assuming that their intersection Ω_0 is not empty (the convex sets are consistent), then Ω_0 is also a closed convex set of H, each point of which satisfies all available information about the solution. Therefore, the image reconstruction problem may be reformulated as the problem of finding a point in a Hilbert space belonging to the intersection of the convex sets defined by a priori information (18). The problem is recursively solvable if a projection operator P_i is realizable for each convex set Ω_i, $i = 1, 2, \ldots, m$. In a Hilbert space, the projection operator onto a convex set maps the image estimate onto the closest point in the associated convex set. The relaxed projection operator T_i can be defined as

$$T_i = I + \lambda_i (P_i - I), \quad [1]$$

where I is the identity operator and λ_i is a relaxation parameter, which affects the convergence speed. If Ω_0 is not empty, and $\lambda_i \in (0,2]$, the fundamental theorem of POCS (17) guarantees weak convergence to a point in Ω_0 by alternating projections onto the sets:

$$g^{(n+1)} = T_m \cdots T_1 g^{(n)}. \quad [2]$$

This method is further referred to as sequential POCS.

Another way to apply convex constraints is to use a parallel (simultaneous) projection technique (26,27). At each iteration of parallel POCS, the result is formed by a combination of the individual results of simultaneous projections onto groups of available sets:

$$g^{(n+1)} = g^{(n)} + \lambda^{(n)} \left(\sum_i w_i P_i(g^{(n)}) - g^{(n)} \right), \quad [3]$$

where $\sum_i w_i = 1$. The $\lambda^{(n)}$ can be chosen the same way as in sequential POCS, or it can be defined as $\lambda^{(n)} \in (0, 2L^{(n)}]$, where $L^{(n)}$ is an iteration-dependent extrapolation parameter used to speed up the convergence (27). Parallel POCS algorithms are more robust than the conventional sequential POCS algorithms in the case of image reconstruction from inconsistent constraints. Inconsistency of the constraints may be caused by noise in the data measurements or systematic errors in constraints. As a rule, the intersection of inconsistent convex sets is an empty set. In this case, the convergence behavior of the sequential and the parallel POCS algorithms is quite different. The sequential algorithm converges to a closed path called a greedy limit cycle and stays on the path indefinitely (Fig. 1a). In cases of inconsistent convex sets, the parallel POCS algorithm converges weakly to a point of a Hilbert space such that the weighted least squares distance between the point and all convex sets is minimized (Fig. 1b). This outcome is preferable because the solution is close to each of the convex sets and, therefore, all constraints on the solution contribute to the result. Additionally, the parallel POCS converges noticeably faster than sequential POCS (26,27).

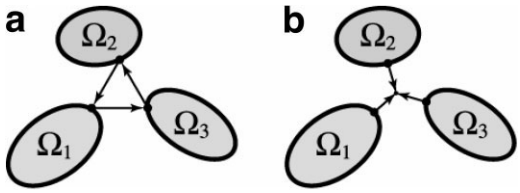

FIG. 1. Convergence of sequential (**a**) and parallel (**b**) POCS algorithms in the case of inconsistent convex sets (the intersection of the convex sets is the empty set).

Convex Sets and Projection Operators for MRI Data Reconstruction

Let r and k denote image space and k-space coordinates, respectively, and let K be a set of k-space positions constituting the sampling trajectory. Assume that $m_0(k)$ is data acquired at $k \in K$. The convex set Ω^{ds} can be defined as a set consisting of all images whose k-space values at $k \in K$ are equivalent to $m_0(k)$. The operator P^{ds} for projection of an arbitrary image function $f(r)$ onto the set Ω^{ds} can be constructed as

$$P^{ds} f(r) = f(r) + \mathrm{IDFT}\{m_0(k) - \mathrm{DFT}_{k \in K}\{f(r)\}\}, \quad [4]$$

where DFT is a discrete Fourier transform mapping data from image domain to k-space sampling trajectory positions, and IDFT is an inverse discrete Fourier transform performing the backward mapping. The operator ensures consistency between reconstructed image and the acquired k-space data. Other convex sets and associated projection operators pertinent to MRI data reconstruction are defined in Table 1.

General Formulation of POCSENSE

Assume that the N_C-element coil array with known coil sensitivities $s_i(r)$, ($i = 1, \ldots, N_C$) is used for the imaging, and $m_{i,0}(k)$ is a data set acquired by the ith coil at $k \in K$ that constitutes the set Ω_i^{ds}. The data projection operator for each set Ω_i^{ds} can be defined in a manner similar to Eq. [4]. In order to guarantee consistency between acquired data and the image to be projected, the image estimate is modulated by the sensitivity profile of the coil element used for the given data set acquisition. The projection operator is then given by

$$P_i^{ds} f(r) = P^{ds}(f(r)s_i(r)) \equiv f(r)s_i(r) + \mathrm{IDFT}\{m_{i,0}(k) - \mathrm{DFT}_{k \in K}\{f(r)s_i(r)\}\}. \quad [5]$$

After the projection, the result should be demodulated by the sensitivity profile. In our method the demodulation is done in Step 2 of the algorithm.

[3]A set $\Omega \in H$ is convex if and only if for any $g_1, g_2 \in \Omega$ and all $\alpha \in [0,1]$ $g = \alpha g_1 + (1 - \alpha) g_2 \in \Omega$.

Table 1
Property Convex Sets and the Associated Projection Operators for MRI Data Reconstruction

Convex set		Projection operator	
Notation	Description	Definition	Description
Ω_M	Set of images with a limited object support M	$P_M g(r) = \begin{cases} g(r), & r \in M \\ 0, & \text{otherwise} \end{cases}$	Zeroes values outside object support M
Ω_v	Set of images with intensity restricted by V ($V>0$)	$P_v g(r) = \begin{cases} g(r), & \lvert g(r)\rvert \le V \\ \dfrac{V \cdot g(r)}{\lvert g(r)\rvert}, & \text{otherwise} \end{cases}$	Restricts the image intensity to be lower or equal to the predefined value V
Ω_ϕ	Set of images with phase equal to $\phi(r)$	$P_\phi g(r) = \lvert g(r)\rvert \cdot e^{i\phi(r)}$	Sets the image phase to the predefined function $\phi(r)$
Ω_E	Set of images with energy in the FOV limited by E ($E>0$)	$P_E g(r) = \begin{cases} g(r)\sqrt{E/E_{\text{FOV}}}, & E_{\text{FOV}} > E, \\ g(r), & \text{otherwise} \end{cases}$ where $E_{\text{FOV}} = \sum_{r \in \text{FOV}} g^2(r)$	Ensures that image energy is not greater than the predefined value E

Additionally, we introduce two families of projection operators based on the image properties (Table 1). The first one is composed of all projections onto sets associated with image property constraints for the image combined of all coil images,

$$P_0^{\text{pr}} \equiv P_{0,N}^{\text{pr}} P_{0,N-1}^{\text{pr}} \cdots P_{0,1}^{\text{pr}}, \quad [6]$$

where N is the number of property constraints onto the image with corresponding projection operators $P_{0,j}^{\text{pr}}$. Property sets can be defined not only for the combined image but also for the individual coil images. The composite projection operator onto these property sets is given by

$$P_i^{\text{pr}} \equiv P_{i,N_i}^{\text{pr}} P_{i,N_i-1}^{\text{pr}} \cdots P_{i,1}^{\text{pr}}, \quad [7]$$

where N_i is the number of constraints onto the ith coil image, and $P_{i,j}$ is a projection operator onto the jth property set of the ith coil image.

Algorithm: POCSENSE

Starting with an initial guess $g^{(0)}(r)$, proceed until convergence as follows:

Step 1:

$$g_i^{(n+1)} = P_i^{\text{pr}} P_i^{\text{ds}}(g^{(n)}), \; i = 1, \ldots, N_C$$

Step 2:

$$t_1 = \sum_{i=1}^{N_C} \alpha_i g_i^{(n+1)}$$

Step 3:

$$t_2 = g^{(n)} + \lambda^{(n)}(t_1 - g^{(n)})$$

Step 4:

$$g^{(n+1)} = P_0^{\text{pr}} t_2.$$

Here, * is the complex conjugate operation, and $g_i^{(n)}$ is the current estimate of the image acquired by the ith coil. Coefficients α_i are precalculated as

$$\alpha_i = \frac{s_i^{(\omega)}}{\sum_{j=1}^{N_C} s_j^{(\omega)} s_j}, \; i = 1, \ldots, N_C. \quad [8]$$

Here,

$$s_i^{(\omega)} = \sum_{j=1}^{N_C} s_j * \omega_{ji}, \; i = 1, \ldots, N_C, \quad [9]$$

where ω_{ij} are entries of the inverse of noise resistance matrix characterizing levels and correlations of noise in the receiver channels (28).

In Step 1, estimates of individual coil images are reconstructed by projecting the current image estimate onto the corresponding data and property convex sets. Then, in Step 2, the updated coil images are combined exploiting the SNR optimal reconstruction equation proposed in Ref. (28). The resulting image estimate is updated in Step 3 and additionally constrained by projecting onto optional property convex sets in Step 4. The diagram in Fig. 2 illustrates the algorithm implementation. The use of property constraints in POCSENSE is possible not only in a sequential (Step 4 of the algorithm) but also in a parallel way (Eq. [3]). Such an approach can reduce sensitivity of solution to errors in constraints (27).

To speed up the algorithm convergence, an iteration-dependent relaxation parameter $\lambda^{(n)}$ may be taken as $0 < \lambda^{(n)} \le 2L^{(n)}$, where $L^{(n)}$ is the extrapolation parameter found as (10)

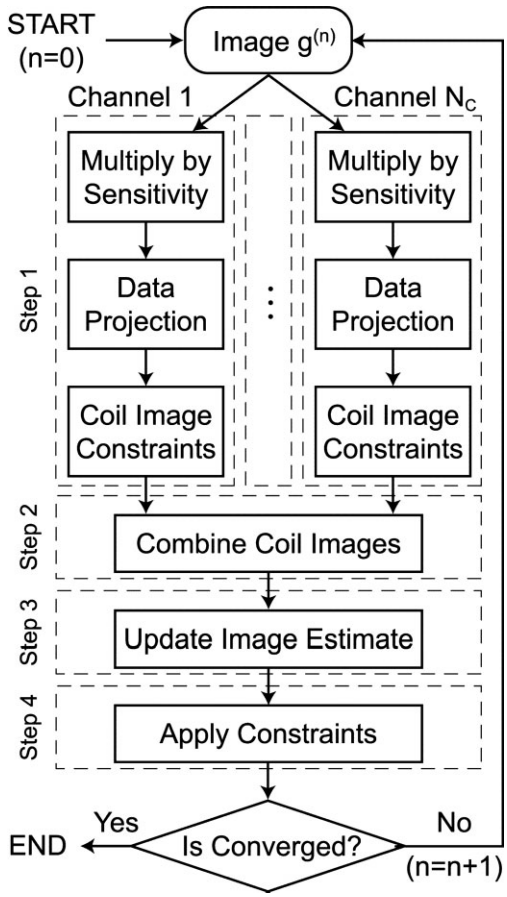

FIG. 2. Block-scheme of POCSENSE.

$$L^{(n)} = \frac{\sum_{i=1}^{N_C} \left\| s_i^{(\omega)} (g_i^{(n+1)} - g^{(n)} s_i) \right\|_2^2}{\left\| \sum_{i=1}^{N_C} s_i^{(\omega)} s_i \cdot (t_1 - g^{(n)}) \right\|_2^2}. \quad [10]$$

Here, $\| \cdot \|_2$ is L2 norm. For nonaccelerated POCSENSE, the parameter $L^{(n)}$ is equal to 1.

MATERIALS AND METHODS

Implementation Details

For the standard POCSENSE reconstruction, coil sensitivity maps and an object mask (object support) were obtained from reference scans by methods similar to those described in Ref. (2). Rough sensitivity maps were obtained as ratios of individual coil images to body coil image and then filtered by polynomial smoothing (quadratic polynomial, Gaussian weighting with $\sigma_s = 0.04$ of image size, window radius $2\sigma_s$). For self-calibrated POCSENSE reconstruction, the coil sensitivities were estimated using the fully sampled central part of *k*-space (29). The following measure,

$$err = \frac{\| g^{(n+1)} - g^{(n)} \|_2}{\| g^{(n)} \|_2}, \quad [11]$$

was chosen as a stopping criterion for POCSENSE iterations. Iterations continue until *err* drops below the predefined value (tolerance). For extrapolated iterations (Eq. [10]), the relaxation parameter was chosen as $\lambda^{(n)} = 1.5\, L^{(n)}$.

POCSENSE implementations for Cartesian and non-Cartesian cases are only different in realization of the data projection operator given in its general form in Eq. [4]. This is the most computationally demanding step of the algorithm as it includes transferring the current image estimate into the *k*-space domain, updating the *k*-space values, and transferring the updated data back into the image space to create a new image estimate. Detailed descriptions for Cartesian and non-Cartesian cases are given below.

Data Projection Operator for Cartesian POCSENSE

The data projection operator for a Cartesian trajectory is equivalent to the data substitution operator used in a POCS-based reconstruction of partial Fourier data (19). The operator implementation could be derived from Eq. [5] resulting in a sequence of operations:

$$\tilde{f}_i(r) = P_i^{ds} f(r) \Leftrightarrow \begin{cases} \text{i. } m_{i,c}(k) = \text{FFT}\{s_i(r) f(r)\} \\ \text{ii. } \tilde{m}_{i,c}(k) = \begin{cases} m_{i,0}(k), k \in K \\ m_{i,c}(k), k \notin K \end{cases} \\ \text{iii. } \tilde{f}_i(r) = \text{IFFT}\{\tilde{m}_{i,c}(k)\} \end{cases} \quad [12]$$

where $m_{i,c}(k)$ is the current estimate of *k*-space data for the *i*th coil image, $i = 1, \ldots, N_C$.

Each projection onto the convex set defined by $m_{i,0}(k)$ includes the fast Fourier transform (FFT) of the image estimate, the update of *k*-space values at the sampled trajectory positions with known values and inverse FFT to the image domain. If the *k*-space data are undersampled only along one dimension, which is typical for 2D P-MRI, a 1D FFT can be used instead of a 2D FFT. The data projection operator implementation is shown in Fig. 3a.

Data Projection Operator for Non-Cartesian POCSENSE

In the case of a non-Cartesian trajectory, the discrete Fourier transforms can be approximated using FFT and *k*-space interpolation (11) or nonuniform FFT (30). The data projection operator for data acquired by the *i*th coil is defined as

$$\tilde{f}_i(r) = P_i^{ds} f(r) \Leftrightarrow \begin{cases} \text{i. } m_{i,c}(k) = \text{FFT}\{s_i(r) f(r)\} \\ \text{ii. } \tilde{m}_{i,c}(k) = m_{i,c}(\text{k}) + G_{AC}(m_{i,0}(k) - G_{CA} m_{i,c}(k)). \\ \text{iii. } \tilde{f}_i(r) = \text{IFFT}\{\tilde{m}_{i,c}(k)\} \end{cases} \quad [13]$$

Here, G_{AC} and G_{CA} are resampling operations transferring the *k*-space data from the original sampling trajectory to a regular Cartesian grid and vice versa. In order to update the *k*-space values, the current Cartesian *k*-space estimate is first resampled onto the original sampling trajectory positions. Then, the difference between initial and updated values is taken to construct a set of error measurements. Finally, the measurements are resampled onto the Cartesian grid and used to construct a new Cartesian *k*-

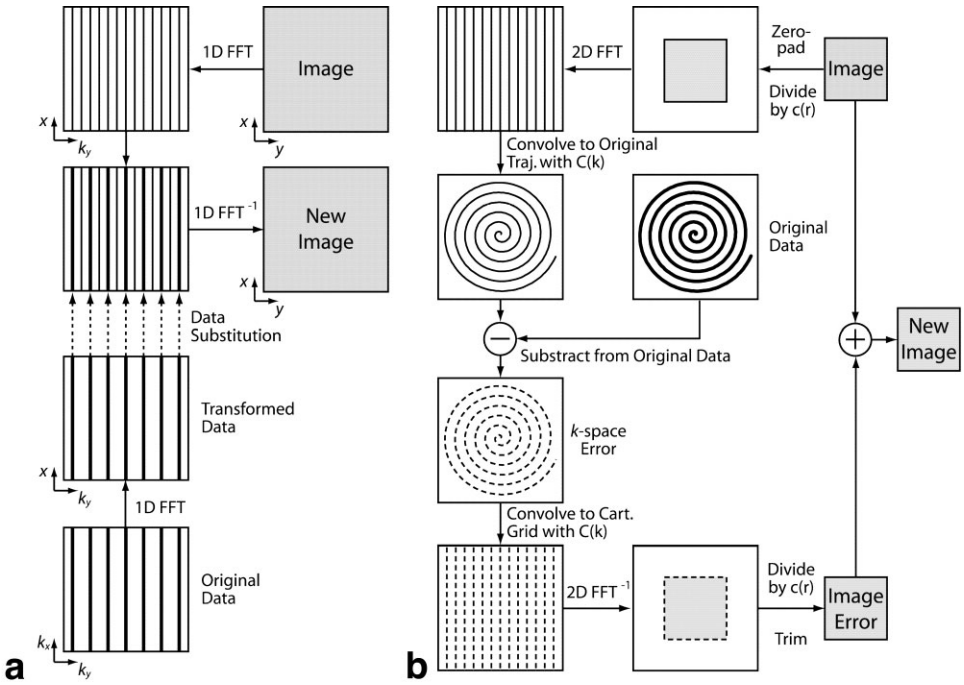

FIG. 3. Implementation of the data projection operator for (**a**) Cartesian and (**b**) non-Cartesian POCSENSE. Here, $C(k)$ is the k-space convolution kernel, and $c(r)$ is its image space counterpart. Sampling density compensation is accomplished before each convolution operation.

space estimate. The diagram in Fig. 3b illustrates the data projection operator implementation for the non-Cartesian case. The described data projection operator could be also used in other POCS-based reconstructions of non-Cartesian MRI data.

To implement the resampling operations, a standard gridding algorithm (31) with Kaiser–Bessel convolution kernel ($L = 3$, $B = 14.1372$) and overgridding by 2 was used. The sampling density compensation function was estimated by a technique described in Ref. (32).

Test Data

POCSENSE was validated by studying its feasibility and effectiveness on synthetic and real data sets. The synthetic data set was constructed using the data from the digital brain phantom (33) as an image magnitude. Image phase was simulated by the quadratic function. The magnitudes of coil sensitivities ($N_C = 4$) were modeled by Gaussian functions and their phase factors by 2D linear functions. Gaussian zero-mean noise was added to both real and imaginary image channels.

Reference and sensitivity encoded images of phantoms were acquired on a 1.5-T Signa MR system (General Electric Medical Systems, Milwaukee, WI) using custom-built bilateral temporal lobe phased array coil (two coil pairs, each coil loop is 9.7 × 11.6 cm) (34). Non-Cartesian data sets were acquired using a spoiled gradient-echo pulse sequence with spiral readout (TE = 3.1 msec, TR = 0.5 sec, flip angle = 45°, FOV = 15 × 15 cm, 2-mm slice thickness, 18 interleaves, 2048 samples per interleave). Cartesian data sets were acquired by imaging the phantoms with fast spin echo pulse sequence (TE = 34 msec, TR = 2 sec, ETL = 16, FOV = 24 × 24 cm, 2-mm slice thickness, matrix = 256 × 256).

Data from healthy volunteers were acquired on a 3-T Trio MR system (Siemens Medical Solutions, Erlangen, Germany) using an eight-channel head coil (MRI Devices, Waukesha, WI) and dual contrast 2D turbo spin echo pulse sequence (TE = 10/100 msec, TR = 5 sec, ETL = 18, FOV = 23 × 23 cm, 2-mm slice thickness, matrix = 256 × 252). Informed consent was obtained from all volunteers in accordance with our institution's human subjects policies.

RESULTS

Unconstrained Reconstruction

Figure 4 shows results of testing POCSENSE on the synthetic data. Two types of sampling, Cartesian and pseudo-random (samples randomly placed on Cartesian grid positions), were considered. The algorithm convergence was measured in terms of RMS error relative to the reference image. Plots demonstrate that reduction of RMS error is accompanied by monotonically decreasing error measure (Eq. [11]). Convergence of POCSENSE and conjugate gradients iterative SENSE (iSENSE) (11) are compared in Fig. 5. For low reduction factors, convergence rates of POCSENSE and iSENSE were comparable. For maximal reduction factor, POCSENSE converged noticeably slower than iSENSE, illustrating the well-known limitation of POCS-based techniques (27) for poorly conditioned cases. However, POCSENSE with adaptive relaxation parameter (Eq. [10]) may be used in such situations to speed up convergence (Fig. 5b).

Figure 6 demonstrates reconstruction of spiral data using POCSENSE and iSENSE (11). To construct an undersampled data set with $R = 2$, every second interleave from an 18-interleave data set was chosen for each coil element of the 4-coil receiver system ($N_C = 4$). The images reconstructed from the complete and undersampled data sets by the gridding technique are shown in Fig. 6a and b, respectively. The quality of the second

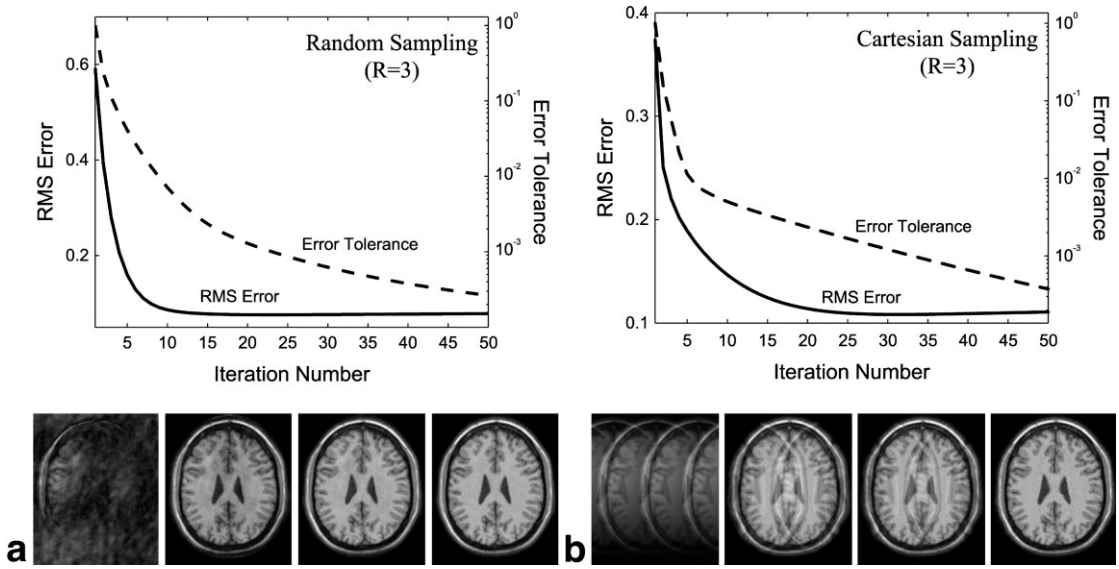

FIG. 4. Reconstruction of the synthetic data set ($R = 3$, $N_C = 4$, $\lambda = 1.5$) for (**a**) pseudo-random and (**b**) Cartesian sampling trajectories. Plots show dependence of error measure and RMS error versus the iteration number. Images illustrate the reconstruction results after the first iteration and after error measure reached values 1e-1, 1e-2, and 1e-3, correspondingly.

image is seriously deteriorated by aliasing artifacts. The POCSENSE reconstructed image (Fig. 6c) is identical to the image reconstructed from the complete data set (Fig. 6a) except for the increased noise level that is characteristic for all P-MRI techniques (Fig. 6d). Noise level was estimated using a central part of the image that was not corrupted by aliasing. In agreement with imaging time reduction by factor of 2 ($R = 2$), noise standard

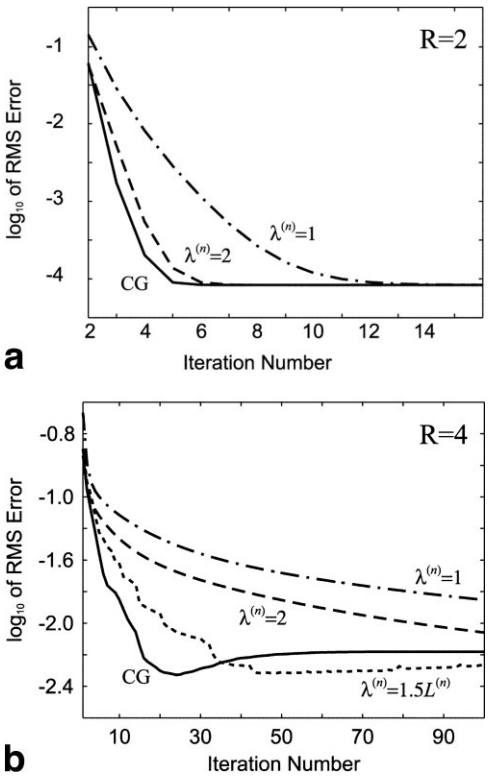

FIG. 5. Convergence of POCSENSE and iSENSE (CG) techniques (digital brain phantom, Cartesian sampling, $N_C = 4$) for (**a**) $R = 2$ and (**b**) $R = 4$.

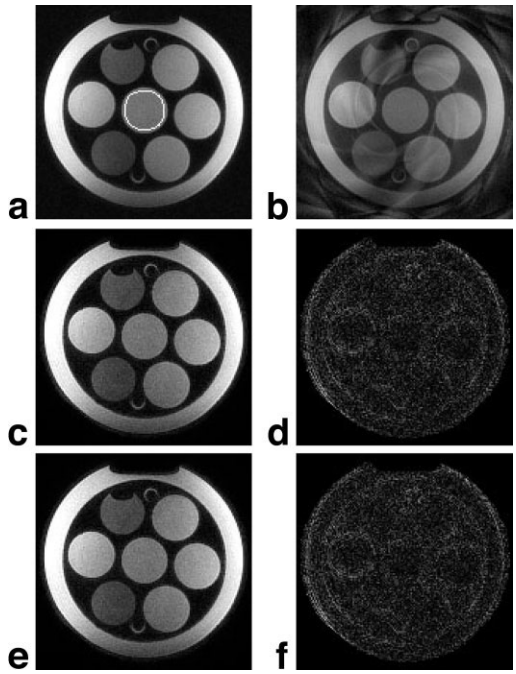

FIG. 6. Application of POCSENSE for non-Cartesian data reconstruction (spiral readout, $R = 2$, $N_C = 4$, tol = 1e-3, $\lambda = 1$, object support constraint). **a**: Reference image (noise SD = 0.032, intensity range [0,1]); white contour in the center identifies ROI for noise estimation. **b**: Sum-of-squares image from gridding reconstruction. **c**, **e**: POCSENSE (SD = 0.0451, RMS = 0.0538) and iSENSE (SD = 0.0452, RMS = 0.0540) images, correspondingly. **d**, **f**: Magnitude of differences between (c, e) and the reference image (a) (intensity range is [0, 0.2]).

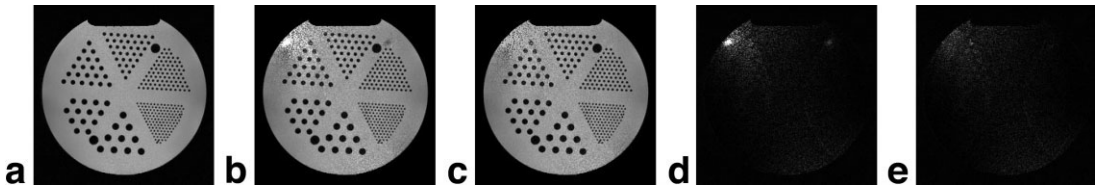

FIG. 7. POCSENSE with MV-constraint. **a**: Reference image. **b**, **c**: Images reconstructed without and using MV constraint, correspondingly. **d**, **e**: Absolute error for (b) and (c), respectively. RMS error for (b) is 0.170 and for (c) is 0.114.

deviation (SD) was approximately increased by the square root of 2. In the absence of additional constraints, POCSENSE and iSENSE produced identical results with similar RMS errors and noise levels.

Constrained Reconstruction

Figure 7 shows the results of a POCSENSE reconstruction of a phantom image from an undersampled Cartesian data set ($R = 2$) obtained with two receiver channels ($N_C = 2$). To estimate the POCSENSE performance with and without maximum value (MV) constraint, we performed the following experiment. First, the upper bound onto image intensity, V, was estimated from the reference image. Then, 50 iterations of POCSENSE without and with MV constraining were computed. The resulting images are shown in Fig. 7b and c, respectively. Differences between reference image reconstructed from fully sampled data (Fig. 7a) and POCSENSE reconstructed images (Fig. 7d and e) reveal that MV constraint can be used to suppress the noise amplification and to improve the image quality.

Figure 8 demonstrates the application of POCSENSE to a solution of underdetermined reconstruction problems. Theoretically, the maximal speedup for P-MRI is equal to the number of coils, N_C. We refer to data sampled with $R \leq N_C$ as highly undersampled, $R = N_C$ as critically undersampled, and $R > N_C$ as overcritically undersampled. A test data set was constructed from the spiral data set by choosing every third interleave. The reduction factor for the resulting data set is equal to 3, which is undercritical for a 4-coil system, but it is overcritical for a 2-coil system. The reconstruction was initially done with 4-coil data set using the gridding technique (Fig. 8a). Then, a reduced 2-coil data set was used to simulate the underdetermined problem. The images reconstructed by the gridding technique and POCSENSE from such a data set are shown in Fig. 8b and c, respectively. Both exhibit significant aliasing artifacts. Finally, POCSENSE, with additional phase constraint, was applied to reconstruct the overcritically undersampled data set. We obtained a phase constraint from the image in Fig. 8a. In practice, this constraint could be obtained in different ways, for example, from the k-space center of variable density spiral data (35). The result of the phase constrained POCSENSE reconstruction is shown in Fig. 8d. The image demonstrates significant improvement in the quality in comparison with the image reconstructed from the same data set but without phase constraining. The residual artifacts in the image center (Fig. 8d) are mainly caused by systematic errors in phase estimate used for phase constraining and are present in the reference image (Fig. 8a) as well. Differences shown in Fig. 8e and f reveal improvement in image quality for phase constrained image reconstruction.

Figure 9 shows an example of self-calibrated POCSENSE reconstruction. In the self-calibration approach (29), the k-space center is fully sampled, while the rest of k-space is undersampled with a reduction factor R (Fig. 9a). Although the effectual reduction factor is reduced in self-calibrated P-MRI, the advantage of such an approach is that coils and image information are acquired in the same scan, ensuring reliability of coil sensitivity estimates. In this study, standard self-calibrated acquisition (Fig. 9a) was simulated from a fully sampled phantom data set. Images reconstructed by self-calibrated POCSENSE for two different numbers of k-space lines used for self-calibration are shown in Fig. 9b and c, respectively. The decreased number of reference k-space lines leads to errors in reconstructed image (Fig. 9d and e).

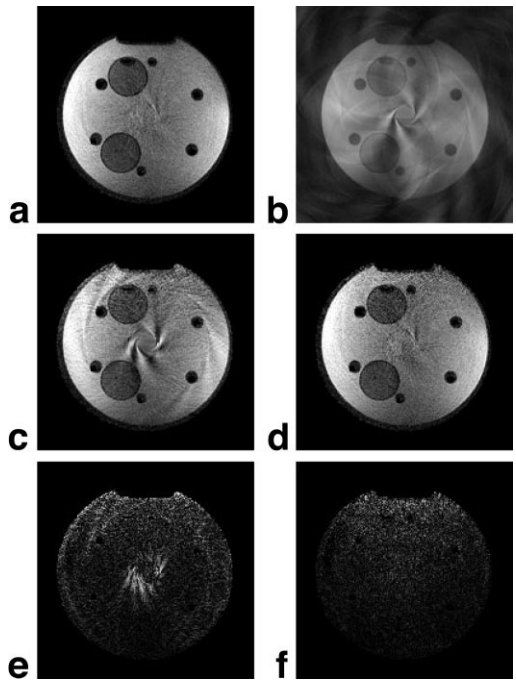

FIG. 8. Application of POCSENSE for overcritically undersampled data reconstruction (spiral readout, 100 iterations, $\lambda = 1$, phase and object support constraints). **a**: Reconstruction of 4-coil data set ($R = 3$, $N_C = 4$). **b**: Sum-of-squares image reconstructed by gridding from 2-coil data set ($N_C = 2$). **c**, **d**: Unconstrained and phase constrained POCSENSE reconstruction of 2-coil data sets ($R = 3$, $N_C = 2$), respectively. **e**, **f**: Magnitude of differences between (c, d) and the reference image (a), correspondingly.

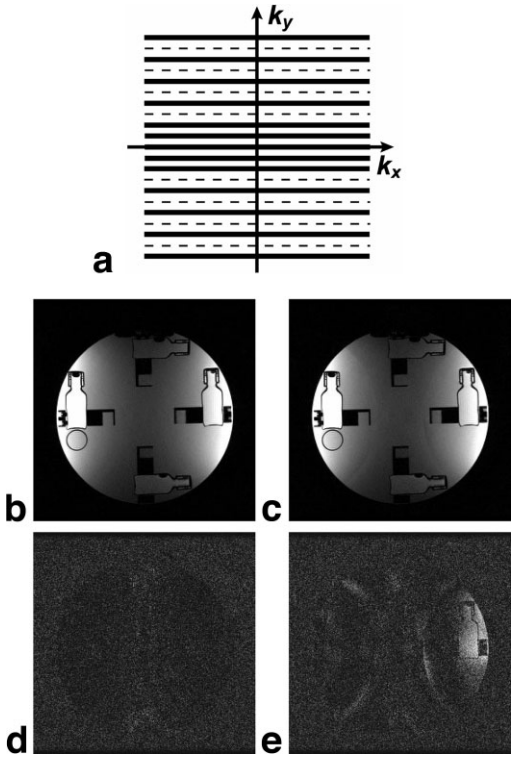

FIG. 9. Self-calibrating POCSENSE reconstruction (Cartesian sampling, $R = 2$, $N_C = 4$, tol = 0.01, $\lambda = 1.5$). **a**: Self-calibrated sampling scheme. **b**, **c**: Reconstruction results for the cases when the number of reference lines for coil estimation was equal to 42 (b) and 22 (c) (total 149 and 139 lines, correspondingly). **d**,**e**: Error images corresponding to (b, c).

Reconstruction of Partial Fourier Data

The partial Fourier (PF) approach has frequently been used to decrease scan time by asymmetrical acquisition of *k*-space (19). Usually, reconstruction of PF data utilizes a low-resolution phase estimate from the symmetrically sampled *k*-space center. PF sampling could be combined with P-MRI (Fig. 10). A standard approach for reconstruction of such data sets is sequential when application of a P-MRI technique is followed by PF reconstruction. These two steps could be combined using phase constrained POCSENSE. In this case, phase estimate from symmetrically sampled *k*-space center is used as a constraint in POCSENSE reconstruction.

Figure 10 demonstrates the results of PF-POCSENSE reconstruction. In this study, the acquisition was simulated using fully sampled real brain data. The sequential approach to PF P-MRI data reconstruction was realized as follows. First, iSENSE was applied to reconstruct the initial image estimate by recovering missing lines in undersampled *k*-space area. Then, the *k*-space estimate was used in POCS-based PF reconstruction (19). PF-POCSENSE used the same phase constraint as the latter procedure. Results indicate that simultaneous utilization of P-MRI and PF significantly improves image quality in comparison with the sequential reconstruction (RMS error is 0.095 versus. 0.165). As with any PF reconstruction, reconstructed images contain errors in the areas where phase estimate deviates from the true image phase. This type of degradation is noticeable on the error images.

DISCUSSION

POCS is a well-known technique for signal reconstruction/recovery from partial or inconsistent data. In recent years, this technique has become widely used by the medical imaging community due to its ability to adapt to a variety of linear and nonlinear constraints in an algorithmically and numerically efficient way (19–25). In this paper, we have demonstrated that the POCS formalism could be suc-

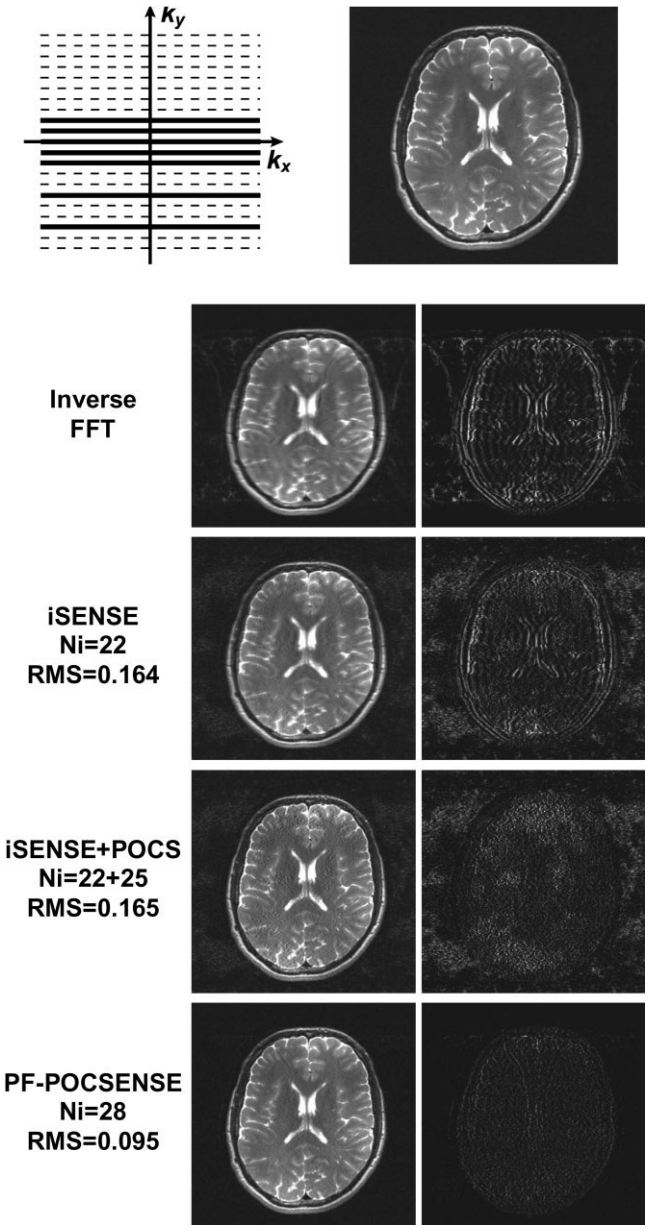

FIG. 10. Comparison of several approaches for PF P-MRI data reconstruction (brain data set, Cartesian sampling, $R = 3$, $N_C = 4$, number of reference lines = 50, tol = 0.001 for all iterative techniques, $\lambda = 1.5$). Top row: PF, self-calibrated P-MRI sampling scheme and reference image from fully sampled data. Bottom rows: images and image errors for different reconstruction approaches.

cessfully employed for P-MRI data reconstruction. The distinctive feature of our new method is that it may easily utilize nontrivial constraints to improve the resulting image quality. Two possible scenarios that involve MV and phase constraints were demonstrated in the Results. Both MV and phase constraints may be obtained from separately acquired reference data or using image estimates from densely sampled regions of such trajectories as radial (36) or a variable-density spiral (35) or utilizing a self-calibrated P-MRI approach.

It was shown that POCSENSE is a flexible tool to combine reconstruction of partial Fourier and P-MRI data in a single procedure. Such a technique results in improved image quality in comparison with a sequential approach (Fig. 10). The observation may be explained by the fact that phase constraining improves conditioning of the P-MRI reconstruction problem, as additional a priori information is included in the reconstruction. PF acquisition is especially suitable for application with self-calibrated P-MRI (37). As such, the image reconstruction becomes self-contained, as it does not require any reference scans for coil sensitivity and image phase estimations. The number of reference lines for PF-POCSENSE should be sufficient to guarantee reliable estimation of coil sensitivities and phase constraint. Too few lines may lead to errors in coils sensitivities and phase constraint deteriorating image quality. If reconstruction relies on coil sensitivity estimates from reference scans, undersampling of central *k*-space area is also applicable. In this case, PF-POCSENSE should be preceded by reconstruction of central *k*-space part for image phase estimation.

POCSENSE is straightforward to implement using standard MR reconstruction methods, such as FFT and gridding algorithms. The reconstruction time per iteration on a laptop PC (AMD 1.8 GHz, 512 Mb RAM) is less than 0.2 sec for Cartesian data and less than 3 sec for spiral data (image matrix = 256×256, $R = 2$, $N_C = 4$, overgridding factor = 2, lookup-table-based implementation of gridding). For many trajectories with oversampled regions, the computationally expensive data projection operator (Eq. [5]) could be implemented using a combination of Cartesian projection (Eq. [12]) for data regridded to regular Cartesian grid positions in oversampled areas and non-Cartesian projection (Eq. [13]) for undersampled areas. As a result, gridding is used only once for the oversampled areas decreasing the computational load of the proposed algorithm. Another interesting way to apply POCSENSE to non-Cartesian data is to utilize the iterative next-neighbor gridding approach, allowing application of efficient Cartesian data projection for data sampled onto arbitrary *k*-space trajectories (38).

The main limitation of POCSENSE is that it exhibits slow convergence for poorly conditioned problems that often arise for highly undersampled data. The use of extrapolated iterations in the POCSENSE implementation partially solves the problem (10). From our experience, extrapolated iterations are most efficient for high reduction factors. The number of iterations required for convergence depends on the choice of the initial guess, relaxation parameter values, the data acquisition reduction factor, sampling strategy, and coil system configuration and may vary among different applications.

Reformulation of the problem of image reconstruction from sensitivity encoded data in the context of the POCS approach presents appealing possibilities for future research. Multiple convex sets introduced by the signal processing community (18,39) may also be adapted for improving P-MRI data reconstruction. Application of low-resolution reference images (16) for constrained POCSENSE reconstruction may be useful to improve reconstruction from highly undersampled data sets and will be considered in separate research. Our algorithm can be easily modified regarding the way property constraints are applied (40). POCSENSE is expected to be equally important for the reconstruction of both Cartesian and non-Cartesian data when nontrivial constraints are available.

REFERENCES

1. Sodickson DK, Manning WJ. Simultaneous acquisition of spatial harmonics (SMASH): fast imaging with radiofrequency coil arrays. Magn Reson Med 1997;38:591–603.
2. Pruessmann KP, Weiger M, Scheidegger MB, Boesiger P. SENSE: Sensitivity encoding for fast MRI. Magn Reson Med 1999;42:952–962.
3. Griswold MA, Jakob PM, Heidemann RM, Haase A. Parallel imaging with localized sensitivities (PILS). Magn Reson Med 2000;44:243–251.
4. Kyriakos WE, Panych LP, Kacher DF, Westin CF, Bao SM, Mulkern RV, Jolesz FA. Sensitivity profiles from an array of coils for encoding and reconstruction in parallel (SPACE RIP). Magn Reson Med 2000;44:301–308.
5. Kellman P, Epstein FH, McVeigh ER. Adaptive sensitivity encoding incorporating temporal filtering (TSENSE). Magn Reson Med 2001;45:846–852.
6. Sodickson DK, McKenzie CA. A generalized approach to parallel magnetic resonance imaging. Med Phys 2001;28:1629–1643.
7. Heidemann RM, Griswold MA, Haase A, Jakob PM. VD-AUTO-SMASH imaging. Magn Reson Med 2001;45:1066–1074.
8. Griswold MA, Jakob PM, Heidemann RM, Nittka M, Jellus V, Wang J, Kiefer B, Haase A. Generalized autocalibrating partially parallel acquisition (GRAPPA). Magn Reson Med 2002;47:1202–1210.
9. Bydder M, Larkman DJ, Hajnal JV. Generalized SMASH imaging. Magn Reson Imaging 2002;47:160–170.
10. Samsonov AA, Kholmovski EG, Johnson CR. Image reconstruction from sensitivity encoded MRI data using extrapolated iterations of parallel projection onto convex sets. Proc SPIE 2003;5032:1829–1838.
11. Pruessmann KP, Weiger M, Bornert P, Boesiger P. Advances in sensitivity encoding with arbitrary *k*-space trajectories. Magn Reson Med 2002;46:638–651.
12. Wang J, Kluge T, Nittka M, Jellus V, Kühn B, Kiefer B. Parallel acquisition techniques with modified SENSE reconstruction mSENSE. First Würzburg Workshop on: Parallel Imaging Basics and Clinical Applications, November 2001.
13. Kellman P, McVeigh ER. SENSE coefficient calculation using adaptive regularization. ISMRM Workshop on Minimum MR Data Acquisition Methods. Marco Island, FL, 2001.
14. Liang ZP, Bammer R, Ji J, Pelc NJ, Glover GH. Making better SENSE: Wavelet denoising, Tikhonov regularization, and total least squares. In: Proceedings of the 10th Annual Meeting of ISMRM, Honolulu, HI, 2002. p 2388.
15. Tsao J, Pruessmann KP, Boesiger P. Feedback regularization for SENSE reconstruction. In: Proceedings of the 10th Annual Meeting of ISMRM, Honolulu, HI, 2002. p 739.
16. Katscher U, Manke D. Underdetermined SENSE using a-priori knowledge. In: Proceedings of the 10th Annual Meeting of ISMRM, Honolulu, HI, 2002. p 2396.
17. Gubin LG, Polyak BT, Raik EV. The method of projections for finding the common point in convex sets. USSR Comput Math Phys 1967;7:1–24.
18. Youla DC, Webb H. Image restoration by the method of convex projections: Part 1, Theory. IEEE Trans Med Imaging 1982;1:81–94.
19. Haacke EM, Lindskog ED, Lin W. A fast, iterative, partial-Fourier technique capable of local phase recovery. J Magn Reson 1991;92:126–145.
20. Liang ZP, Boada FE, Constable RT, Haacke EM, Lauterbur PC, Smith MR. Constrained reconstruction methods in MR imaging. Rev Magn Reson Med 1992;4:67–185.

21. McGibney G, Smith MR, Nichols ST, Crawley A. Quantitative evaluation of several partial Fourier reconstruction algorithms used in MRI. Magn Reson Med 1993;30:51–59.
22. Hedley M, Yan H, Rosenfeld D. An improved algorithm for 2D translational motion artifact correction. IEEE Trans Med Imaging 1991;10: 548–553.
23. Weerasinghe C, Yan H. An improved algorithm for rotational motion artifact suppression in MRI. IEEE Trans Med Imaging 1998;17:310–317.
24. Kholmovski EG, Samsonov AA, Parker DL. Motion artifact reduction technique for dual-contrast FSE imaging. Magn Reson Imaging 2002; 20:455–462.
25. Lee KJ, Barber DC, Paley MN, Wilkinson ID, Papadakis NG, Griffiths PD. Image-based EPI ghost correction using an algorithm based on projection onto convex sets (POCS). Magn Reson Med 2002;47:812–817.
26. Pierra G. Decomposition through formalization in a product space. Math Programming 1984;28:96–115.
27. Combettes PL. Convex set theoretic image recovery by extrapolated iterations of parallel subgradient projections. IEEE Trans Image Processing 1997;6:493–506.
28. Roemer PB, Edelstein WA, Hayes CE, Souza SP, Mueller OM. The NMR phased array. Magn Reson Med 1990;16:192–225.
29. McKenzie CA, Yeh EN, Ohliger MA, Price MD, Sodickson DK. Self-calibrating parallel imaging with automatic coil sensitivity extraction. Magn Reson Med 2002;47:529–538.
30. Sarty GE, Bennet R, Cox RW. Direct reconstruction of non-Cartesian k-space data using a nonuniform fast Fourier transform. Magn Reson Med 2001;45:908–915.
31. Jackson JI, Meyer CH, Nishimura DG, Macovski A. Selection of a convolution function for Fourier inversion using gridding. IEEE Trans Med Imaging 1991;10:473–478.
32. Pipe JG, Menon P. Sampling density compensation in MRI: rationale and an iterative numerical solution. Magn Reson Med 1999;41:179–186.
33. Collins DL, Zijdenbos A, Kollokian V, Sled JG, Kabani NJ, Holmes CJ, Evans AC. Design and construction of a realistic digital brain phantom. IEEE Trans Med Imaging 1998;17:463–468.
34. Hadley JR, Chapman BE, Roberts JA, Chapman DC, Goodrich KC, Buswell HR, Alexander AL, Tsuruda JS, Parker DL. A three-coil comparison for MR angiography. J Magn Reson Imaging 2000;11:458–468.
35. Spielman DM, Pauly JM, Meyer CH. Magnetic resonance fluoroscopy using spirals with variable sampling densities. Magn Reson Med 1995; 34:386–394.
36. Glover GH, Pauly JM. Projection reconstruction techniques for reduction of motion effects in MRI. Magn Reson Med 1992;28:275–289.
37. Bydder M, Robson MD. Partial Fourier partially parallel imaging. In: Proceedings of the 12th Annual Meeting of ISMRM, Kyoto, Japan, 2004. p. 532.
38. Moriguchi H, Duerk JL. POCSENSE using INNG (POCSENSINNG): An efficient reconstruction method for sensitivity encoding with nonuniformly sampled k-space data. In: Proceedings of the 11th Annual Meeting of ISMRM, Toronto, Canada, 2003.
39. Combettes PL, Trussell HJ. The use of noise properties in set theoretic estimation. IEEE Trans Signal Proc 1991;39:1630–1641.
40. Combettes PL, Bondon P. Hard-constrained inconsistent signal feasibility problems. IEEE Trans Signal Proc 1999;47:2460–2468.